

Boundary influence on the fields and arrangement of the needle domains in barium titanate single crystals^{*}

D. Sui^a, John E. Huber^{b,*} and Jie Zhou^a

^a*School of Aeronautics, Northwestern Polytechnical University, Xi'an, Shaanxi, China*

^b*Department of Engineering Science, University of Oxford, Parks Road, Oxford, OX1 3PJ, UK*

ARTICLE INFO

Keywords:

ferrelectric
domain
barium titanate
boundary

ABSTRACT

The superposition theory is adopted to study the boundary value problem of needle domains in barium titanate single crystals, which decomposes into an infinite-medium solution and a complementary solution. The model of an equivalent edge dislocation and line charge is adopted to calculate the fields due to the discrete needle domains in an infinite medium. The complementary solutions are obtained from a linear elastic boundary value problem using the finite element method. The influence of boundaries on the fields and arrangement of the needles in thin barium titanate single crystals is analysed, by considering traction-free boundaries and using the plane stress approximation. According to the principle of minimum potential energy, it is found that pairs of parallel needle domains can be stabilized if the effective charge associated with the needle tips is reduced to 48% of the material's full polarization charge. The evolution of comb-like arrays of needle domains under compressive mechanical load is simulated, and the results are found to be qualitatively similar to experimental observations which have not previously been explained theoretically.

1. Introduction

Barium titanate (BaTiO₃) single crystals, as lead-free ferroelectric materials, possess high polarization and can achieve large electrostrictive strains. Thus they can be used to improve the performance of a variety of transducers. However, the existence of needle domains in single crystals influences the domain switching and the working performance in applications, due to the associated stress and electrical fields around the needle domains. Additionally, common domain patterns such as laminar structure develop through the growth of groups of needle domains. Therefore, improved understanding of the behaviour of needle domains is of importance for the application of this material.

Needle domains are a common feature in a variety of ferroelectrics Salje and Ishibashi (1996); Blackburn and Salje (1999); Harrison et al. (2004); Tagantsev et al. (2010). They comprise thin layers of one domain type embedded in a surrounding matrix of another domain; seen edge-on, such layers appear as fine “needles”, each terminating within the crystal at a “needle-tip”. They are sensitive to temperature, stress and electric fields and are usually generated upon cooling through the Curie temperature during the production of single crystals. In this case, the formation of a needle domain allows straining, such as differential thermal contraction, to be accommodated. During the service lifetime of a BaTiO₃ single crystal, needle domains are influenced by external mechanical loads, usually responding to stress by longitudinal extension or retraction, without sideways motion. **The generation of needle domains can be achieved in a controlled way in the laboratory through temperature variation or applied mechanical loads. It is significant to understand the mechanics of how needle domains arrange and how they respond to external loads. Thus there is a need for a model that can solve boundary value problem for a ferroelectric containing needle domains.**

Researchers have investigated the behaviour of needle-shaped domains over decades using both theoretical and experimental methods. Bornarel et al. (Bornarel and Lajzerowicz (1968); Bornarel (1972)) built a model of effective dislocations to analyse the interaction of needle domains in ferroelectric KH₂PO₄, and

^{*}This document is the results of the research project funded by EPSRC of UK Grant EP/g065233/1 and the Fundamental Research Funds for the Central Universities of China under Grant No. G2019KY05207.

^{*}Corresponding author

✉ suidan@nwpu.edu.cn (D. Sui); john.huber@eng.ox.ac.uk (J.E. Huber)

experimentally confirmed the existence of long-range interaction ($\sim 200\mu\text{m}$) of domains. The dynamic response of needle domains in LaAlO_3 single crystals under weak elastic stress was investigated through optical observation and thermodynamic analysis, see Harrison et al. (2004); Harrison and Salje (2010). They mainly concentrated on the propagation of needle domains rather than the sideways movements of domain walls, which happened only at higher loading levels. It was found that the propagation of a single ferroelastic needle domain under weak elastic stress consisted of two parts: a continuous front propagation and jerky avalanches. Nataf and Salje (2020) observed similar evolution of needle domains including jerky and avalanche motion, as well as gradual motion. Salje (2021) reviewed needle domain movement under field and applications for ferroelectric needle domains, including transport properties for electronic and chemical currents, and the possibility of neuromorphic computing. Using transmission electron microscopy, highly charged needle domain tips were found in lead titanate, where they meet an opposing 180° , see Moore et al. (2020). Liu et al. (2020) used X-ray Bragg coherent diffractive imaging in conjunction with Landau theory to identify the 3D structure of needle domains in barium titanate nanocrystals and also studied the behavior and evolution of needle domains under external tensile and compressive stress. Lich and Dinh (2019) proposed an improved phase field model to investigate the formation, local interactions, and flexoelectric effects of needle-like domains with curved domain walls in lead zirconate titanate (PZT) thin films. Thus needle domains have been studied in a wide variety of configurations and shown to play a key role in ferroelectric switching mechanisms.

In other research, it has been found that needle shaped domains appeared during the development of microstructural features, including in thin films (Matsumoto and Okamoto (2010)). Fang et al. (2007) and Neumeister et al. (2010) found that needle domains accompany the development of crack propagation, appearing ahead of the crack tip. Li *et al.* adopted a phase-field model to investigate the nucleation and growth of needle domains near a stationary crack tip in a single crystal of ferroelectric material (Li and Landis (2011, 2010)). Carka and Landis (2012) further considered a phase-field model with periodic boundary conditions to simulate the fields due to needle-shaped domains. Others have observed 90° a-a needle domains using transmission electron microscopy (TEM) when they investigated the switching mechanism of multi-domains in BaTiO_3 single crystal, see Zhang et al. (2008, 2006); Qi et al. (2006). The existence of needle-shaped domains gives rise to high local stresses and electrical fields around the needle tips. Where the tips of comb-like groups of needle domains terminate, the high stress state at the tip front can also induce the growth of cracks. Thus, the evolution of needle domains under the external loading is of significance to the failure mechanisms of ferroelectric materials.

Most studies of needle domains use experimental observation or modelling at the nano-scale, but relatively few models have been proposed to explain their observed macroscopic patterning and evolution. **In this paper, a semi-analytical model is developed, using effective dislocation and line charge to represent the fields around needle domains. This is then built into a finite element model to study boundary value problems in finite crystals, using superposition theory. Both material anisotropy and electromechanical coupling are taken into account. The model is used to analyse the behaviour of needle domains in finite crystals with external loads, which is a development from our previous research Sui and Huber (2020). In previous research, we found that, in an infinite crystal, needle domain patterns were typically unstable due to strong electric fields near the needle-tips. When the local effective space charge density was reduced sufficiently in the model, stable patterns of needle domains emerged, and these appeared consistent with experimental observation. In the present work, when the influence of boundaries is considered, we test the validity of the previous findings near free surfaces. The influence of boundaries on the local fields and on the arrangement of the needle domains is studied and discussed, along with the evolution of needle domains under mechanical loading.**

2. Theory

2.1. Superposition theory

This paper focuses on the study of 90° a-a type needle domains, whose formation results from 90° switching. As shown in Fig. 1(a), the two sidewalls of the needle domain are 90° domain walls, **and satisfy the corresponding electrical and mechanical compatibility requirements.** However, the incompatible jumps in spontaneous polarization and strain near the needle domain tip imply the existence of local stress and electric fields to restore compatibility. The stresses and electric fields due to this kind of needle domain

can be approximated as those due to an effective edge dislocation coupled with line charge (Sui and Huber (2020)). As illustrated in Fig. 1(b), the needle domain is then represented by an edge dislocation (\perp) and a line charge (\oplus or \ominus). The direction of Burgers vector, \mathbf{b} , and the sign of the line charge, Q , are determined by the relation of the polarization directions between parent domain and needle domain. Their magnitudes are proportional to the needle width, and the magnitudes of lattice strain and polarization. Both electromechanical coupling and crystalline anisotropy are taken into account, but the model is an approximation in which we treat the material surrounding each needle tip as a homogeneous domain. This neglects the inhomogeneity due to the material of the needle itself, and similarly neglects inhomogeneity due to other needles in the vicinity. For thin and relatively widely spaced needles, the influence of this inhomogeneity is likely to be much less significant than the effects due to the equivalent dislocation and line charge.

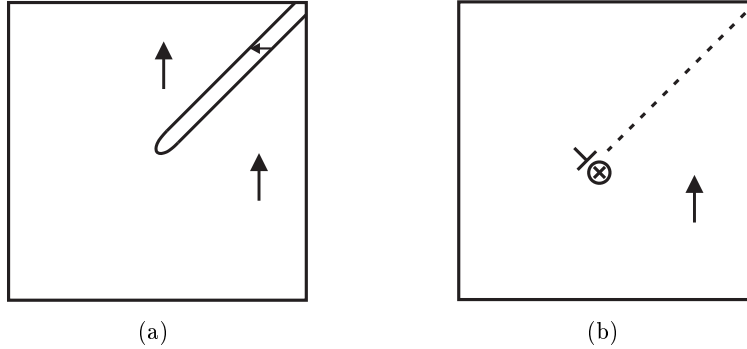


Figure 1: (a) 90° a-a type needle domain terminating within a thin barium titanate single crystal; arrows indicate the polarization direction; (b) The electromechanical fields of the needle domain are modelled as those due to an effective edge dislocation and a line of charges.

The constitutive equations for a piezoelectric medium describing the relationship of mechanical stress σ_{ij} and electrical displacement D_i with the displacement gradients $u_{k,m}$ and the electric potential gradients $\varphi_{,m}$ are

$$\sigma_{ij} = C_{ijk m} u_{k,m} + e_{mij} \varphi_{,m} \quad (1)$$

$$D_i = e_{ikm} u_{k,m} - \kappa_{im} \varphi_{,m} \quad (2)$$

where $C_{ijk m}$, e_{mij} , and κ_{im} are the tensors of elastic, piezoelectric, and dielectric constants, respectively. Additionally, the relation between electric potential φ and electric field E_i is

$$E_i = -\partial\varphi/\partial x_i = -\varphi_{,i} \quad (3)$$

The equilibrium equations, in the absence of body forces and free charge are given by

$$\sigma_{ij,i} = 0 \quad D_{i,i} = 0 \quad (4)$$

Superposition theory is used to calculate the fields due to the needle domains in the presence of a finite boundary. As illustrated in Fig. 2, the initial problem, which is considered to be subjected to traction T_0 on surface portion S_f , displacement U_0 on S_u , charge q_0 on S_q and electric potential ϕ_0 on S_ϕ , can be decomposed into the singular fields (\sim) without boundary conditions and the image field (\wedge) as a complementary solution. The displacement, stress, electric potential and electric displacement fields of the original problem are thereby written as

$$u_i = \tilde{u}_i + \hat{u}_i \quad (5a)$$

$$\sigma_{ij} = \tilde{\sigma}_{ij} + \hat{\sigma}_{ij} \quad (5b)$$

$$\varphi_i = \tilde{\varphi}_i + \hat{\varphi}_i \quad (5c)$$

$$D_i = \tilde{D}_i + \hat{D}_i \quad (5d)$$

The corresponding strain $\varepsilon_{ij} = (u_{i,j} + u_{j,i})/2$, and electric fields E_i , can be calculated by constitutive Eqs. (1) and (2). The (\sim) fields are the superposition fields associated with the individual needles, keeping their

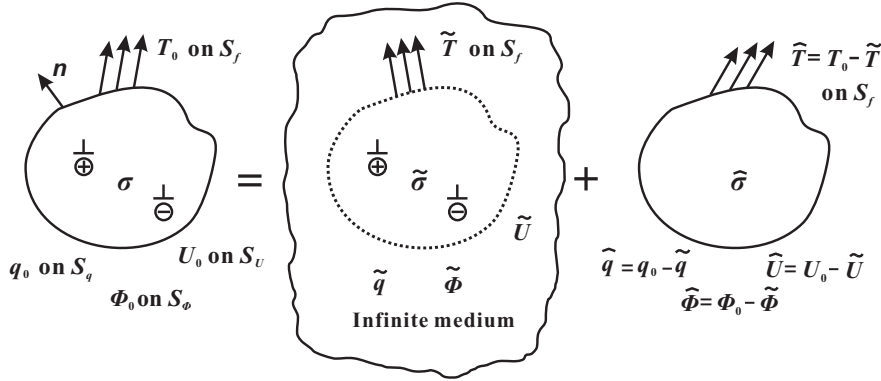


Figure 2: Decomposition of the boundary value problem into the sum of the singular (\sim) fields associated with the individual needles and the image (\wedge) fields that enforce the prescribed boundary conditions.

current configuration but in an infinite medium. For a set of N needles,

$$\tilde{\varepsilon}_{ij} = \sum_{J=1}^N \tilde{\varepsilon}_{ij}^{(J)}, \quad \tilde{\sigma}_{ij} = \sum_{J=1}^N \tilde{\sigma}_{ij}^{(J)}, \quad \tilde{E}_i = \sum_{J=1}^N \tilde{E}_i^{(J)}, \quad \tilde{D}_i = \sum_{J=1}^N \tilde{D}_i^{(J)} \quad (6)$$

where, $\tilde{\varepsilon}^{(J)}$, $\tilde{\sigma}^{(J)}$, $\tilde{E}^{(J)}$ and $\tilde{D}^{(J)}$ represent the strain, stress, electric field and electric displacement of the J^{th} needle domain in an infinite medium, respectively.

The generalized displacement gradient for each needle domain is then provided by Barnett and Lothe (1975) as:

$$u_{I,m} = (2\pi |\mathbf{x}|)^{-1} \{ -m_m(S_{IS}b_S + Q_{IS}q_S) + n_m(nn)_{IJ}^{-1} [(4\pi B_{JS} + (nm)_{JK}S_{KS})b_S + (S_{SJ} + (nm)_{JK}Q_{KS})q_S] \} \quad (7)$$

where lower-case indices run from 1 to 3 while upper-case indices run from 1 to 4, such that $u_I (I = 1 \cdots 3)$ is the displacement vector and u_4 is the electric potential. The 4×4 matrices \mathbf{S} , \mathbf{Q} and \mathbf{B} are related to the material constants, see Appendix. Plane basis vectors \mathbf{m} and \mathbf{n} are defined such that $\mathbf{m} \cdot \mathbf{x} = |\mathbf{x}|$ and $\mathbf{n} \cdot \mathbf{x} = 0$, and the components of the 4×4 matrices (\mathbf{nn}) and (\mathbf{nm}) are defined in the appendix. Having computed strain and electric field using Eq. (7), the corresponding stress and electric displacement fields are directly obtained from constitutive Eqs. (1) and (2). The values at the actual boundary S are:

$$\tilde{\sigma}_{ij}n_j = \tilde{T} \quad \text{on } S_f \quad (8)$$

$$u = \tilde{U} \quad \text{on } S_u \quad (9)$$

$$\tilde{D}_i n_i = -\tilde{q} \quad \text{on } S_q \quad (10)$$

$$\varphi = \tilde{\phi} \quad \text{on } S_\phi \quad (11)$$

where, n is the outer unit normal to boundary S , and $S = S_u \cup S_f$, $S = S_q \cup S_\phi$. These boundary conditions facilitate the solution of the image field.

In the (\sim) field, the sum of the individual needle fields does not in general satisfy the prescribed boundary conditions. The image (\wedge) fields are used to correct for the actual boundary conditions by solving the image problem in a region with no dislocations or line charges. Since the (\wedge) fields are smooth and continuous fields without singularities, the boundary value problem can be solved by any convenient numerical method such

as the finite element method or the boundary element method. Here, we adopt the finite element method to obtain the complementary solution. The boundary loads of the image (\wedge) fields are:

$$\widehat{T} = T_0 - \widetilde{T} \quad (12)$$

$$\widehat{U} = U_0 - \widetilde{U} \quad (13)$$

$$\widehat{q} = q_0 - \widetilde{q} \quad (14)$$

$$\widehat{\phi} = \phi_0 - \widetilde{\phi} \quad (15)$$

The total potential energy combines contributions from strain energy, electrical energy, and traction or charge imposed on the boundary:

$$U_E = \frac{1}{2} \int_v (\sigma \cdot \varepsilon + E \cdot D) dv - \int_{S_f} T_0 \cdot U ds - \int_{S_q} \phi \cdot q_0 ds \quad (16)$$

Variations of the total potential energy can be considered in order to find a steady equilibrium pattern formed by the needle domains.

A modified Peach-Koehler force is computed to quantify the interaction forces between needle domains, which is critical to their evolution. This is calculated by:

$$F_m^{(I)} = \epsilon_{ilm} k_l (\widehat{\sigma}_{ij} + \sum_{J \neq I}^N \widetilde{\sigma}_{ij}^{(J)}) b_j^{(I)} + (\widehat{E}_m + \sum_{J \neq I}^N \widetilde{E}_m^{(J)}) q^{(I)} \quad (17)$$

where, $F_m^{(I)}$ represents the components of the force acting on the needle N_I ; $F_m^{(I)}$ can be resolved along the direction of needle extension to provide the thermodynamic driving force for needle growth. The needle domain N_I is modelled as an edge dislocation of Burgers vector $\mathbf{b}^{(I)}$ coupled with a line charge $q^{(I)}$. Here, ϵ is the permutation tensor, \mathbf{k} is the out-of-plane unit vector along the x_3 co-ordinate axis, and N is the total number of interactive needles. The existence of each needle domain produces stress and electric fields that can be superposed.

2.2. Plane stress and plane electric displacement formulation

The crystal plate is modelled as a thin sheet of material lying in a plane normal to the x_3 axis. Thus there is a free surface normal to x_3 and due to insulating properties this surface is largely free of charge. Consequently, plane stress and plane electric displacement become appropriate model approximations, reducing the model to a 2-dimensional system in the x_1 - x_2 plane. Barnett's solution provides a plane strain and plane electric field result for the infinite-medium problem. In this section, we briefly review relationships to transform between plane strain-plane electric field conditions and plane stress-plane electric displacement. For convenience, the constitutive equations modified from Eqs. (1) and (2), which describe the relationship of mechanical stress σ and electric displacement \mathbf{D} with the strain ε and the electric field \mathbf{E} , are given in matrix form by:

$$\begin{bmatrix} \sigma \\ \mathbf{D} \end{bmatrix} = \begin{bmatrix} \mathbf{C} & -\mathbf{e} \\ \mathbf{e} & \kappa \end{bmatrix} \begin{bmatrix} \varepsilon \\ \mathbf{E} \end{bmatrix} \quad (18)$$

with sub-matrices \mathbf{C} , \mathbf{e} , and κ representing the elastic, piezoelectric, and dielectric properties, respectively. The inverse of Eq. (18) is:

$$\begin{bmatrix} \varepsilon \\ \mathbf{E} \end{bmatrix} = \begin{bmatrix} \mathbf{S}^D & \mathbf{g} \\ -\mathbf{g} & \beta^\sigma \end{bmatrix} \begin{bmatrix} \sigma \\ \mathbf{D} \end{bmatrix} \quad (19)$$

In plane stress and plane electric displacement, all stress and electric displacement components perpendicular to the plane (x_1, x_2) are taken to be zero; the remaining nonzero components are σ_1 , σ_2 , σ_6 , and D_1 , D_2 , using the standard Voigt notation. Therefore, Eq. (19) is reduced to:

$$\begin{bmatrix} \varepsilon_1 \\ \varepsilon_2 \\ \varepsilon_6 \\ E_1 \\ E_2 \end{bmatrix} = \begin{bmatrix} S_{11}^D & S_{12}^D & S_{16}^D & g_{11} & g_{12} \\ S_{21}^D & S_{22}^D & S_{26}^D & g_{21} & g_{22} \\ S_{61}^D & S_{62}^D & S_{66}^D & g_{61} & g_{62} \\ -g_{11} & -g_{12} & -g_{16} & \beta_{11}^\sigma & \beta_{12}^\sigma \\ -g_{21} & -g_{22} & -g_{26} & \beta_{12}^\sigma & \beta_{22}^\sigma \end{bmatrix} \begin{bmatrix} \sigma_1 \\ \sigma_2 \\ \sigma_6 \\ D_1 \\ D_2 \end{bmatrix} \quad (20)$$

Table 1

Material constants of BaTiO₃ in the tetragonal phase with polarization direction [0 1 0] Burcsu et al. (2004); Li et al. (1991); Bhattacharya and Ravichandran (2003)

	BaTiO ₃ single crystal
Structure	Tetragonal (<i>4mm</i>)
Spontaneous polarization, p_0 (C/m ²)	0.26 (25°C)
Spontaneous strain, ε_0	0.0073 (20°C)
Elastic stiffness, C (GPa)	211(C_{11}), 114(C_{12}), 107(C_{13}), 160(C_{22}), 56.2(C_{44}), 127(C_{55}) (25°C)
Piezoelectric coefficients, e (C/m ²)	32.6(e_{16}), -3.88(e_{21}), 5.48(e_{22}) (25°C)
Dielectric constants, κ	1980(κ_{11}/κ_0), 48(κ_{22}/κ_0), $\kappa_0 = 8.854 \times 10^{-12}$ (F/m) (25°C)

The corresponding inverse of Eq. (20) is given by:

$$\begin{bmatrix} \sigma_1 \\ \sigma_2 \\ \sigma_6 \\ D_1 \\ D_2 \end{bmatrix} = \begin{bmatrix} C_{11}^* & C_{12}^* & C_{16}^* & -e_{11}^* & -e_{12}^* \\ C_{21}^* & C_{22}^* & C_{26}^* & -e_{21}^* & -e_{22}^* \\ C_{61}^* & C_{62}^* & C_{66}^* & -e_{61}^* & -e_{62}^* \\ e_{11}^* & e_{12}^* & e_{16}^* & \kappa_{11}^* & \kappa_{12}^* \\ e_{21}^* & e_{22}^* & e_{26}^* & \kappa_{12}^* & \kappa_{22}^* \end{bmatrix} \begin{bmatrix} \varepsilon_1 \\ \varepsilon_2 \\ \varepsilon_6 \\ E_1 \\ E_2 \end{bmatrix} \quad (21)$$

Eq. (21) and Eq. (18) have the same form, the only difference being in the coefficients relating certain stress (or electric displacement) and strain (or electric field) components. It should be noted that the transform in general affects all of these coefficients, so that matrix methods should be used. The plane stress-plane electric field solution is then identical to a plane strain-plane electric displacement solution for a material with different material constants, as given in Eq. (21).

3. Applications of the model

3.1. Basic information

Material constants for a BaTiO₃ single crystal in the tetragonal phase with polarization direction [0 1 0] are given in Table 1. Non-dimensionalization is applied to make the results independent of physical dimensions, and to avoid numerical instability during the computing process. We choose characteristic parameters including the spontaneous polarization magnitude p_0 (0.26 C/m²), spontaneous strain magnitude ε_0 (0.0073), a characteristic electric field magnitude E_0 (0.1×10^6 V/m) and the width of a typical needle domain w (10 μ m). The constitutive Eqs. (1) and (2) are non-dimensionalized as:

$$\frac{\sigma}{\sigma_0} = \left(\frac{C\varepsilon_0}{\sigma_0} \right) \frac{\varepsilon}{\varepsilon_0} - \left(\frac{eE_0}{\sigma_0} \right) \frac{E}{E_0}, \quad \sigma^* = C^*\varepsilon^* - e^*E^* \quad (22)$$

$$\frac{D}{p_0} = \left(\frac{e\varepsilon_0}{p_0} \right) \frac{\varepsilon}{\varepsilon_0} + \left(\frac{\kappa E_0}{p_0} \right) \frac{E}{E_0}, \quad D^* = e^{**}\varepsilon^* + \kappa^*E^* \quad (23)$$

where the dimensionless variables are defined as σ^* , D^* , ε^* , E^* , C^* , e^* , e^{**} and κ^* . To make the dimensionless piezoelectric constants $e^* = e^{**}$, a characteristic stress $\sigma_0 = E_0 p_0 / \varepsilon_0 = 3.56$ MPa is used. Additionally, the generalized Burgers vector $\mathbf{b} = [b_1, b_2, b_3, \Delta\varphi]^T$ components are normalized by $\varepsilon_0 w$ ($i = 1 \dots 3$) and $E_0 w$ ($i = 4$). The generalized line charge vector $\mathbf{q} = [0, 0, 0, q]^T$ is similarly normalized using $p_0 w$. For the 90° a-a needle, the resulting magnitude of effective dislocation and line charge produced by the mechanical and electrical incompatibility at the needle domain tip are $3\varepsilon_0 w$ and $q = \sqrt{2}p_0 w$.

The boundary value problem with free traction ($T_0 = 0$) and zero potential ($\phi_0 = 0$) is used to validate the model in a finite case, by comparison with the infinite (no boundaries) case. A square crystal plate of size $500w \times 500w$ is modelled. According to the above superposition theory, the boundary value problem is decomposed into two parts: (1) infinite solution; (2) complementary solution. The boundary loads are

prescribed or computed as follows:

- (1) The original problem: $T_0 = 0$, $\phi_0 = 0$
- (2) Infinite part (\sim): $\tilde{T} = \tilde{\sigma}_{ij}n_j$, $\tilde{\phi} = \varphi$, computed from solution of the (\sim) problem
- (3) Complementary part (\wedge): $\hat{T} = T_0 - \tilde{T}$, $\hat{\phi} = \phi_0 - \tilde{\phi}$

In the (\sim) field, the solution of the stress $\tilde{\sigma}$ and electric potential $\tilde{\phi}$ is computed by the model of effective dislocation and line charge. The corresponding stress field and electric field are superposed from each discrete dislocation and line charge, as calculated by Eq. (6). Additionally, the boundary condition on the virtual edge \tilde{S} is found for use in the complementary problem. The complementary (\wedge) problem is solved using the finite element method in the commercial software ABAQUS. The $500w \times 500w$ region was meshed using 4-node bilinear plane-stress piezoelectric quadrilateral elements, CPS4E. Due to the regular shape, structured meshing was adopted to generate a structured mesh with the element size $1w \times 1w$. The 4-node shape function was used to interpolate the solution between the discrete values obtained at the mesh nodes.

3.2. The influence of the effective line charge

Based on the previous study of Sui and Huber (2020), the equilibrium configuration of needle domains is sensitive to the quantity of effective charge at the needle tip. It was found, in the infinite case, that there was no stable equilibrium configuration for a pair of parallel similar needle domains if the line charge magnitude Q was greater than $0.73q$ where $q = \sqrt{2}p_0w$. A minimum potential energy configuration for two parallel interacting needle domains was found with $Q = 0.48q$. To analyse the sensitivity of the equilibrium configuration to line charge in the presence of boundaries, a pair of identical needle domains (N_1 & N_2) oriented at 45° to the x_1 positive direction are chosen, as illustrated in Fig. 3. The polarization direction of the parent domain and needle domain are $\mathbf{P}^1 = [0 \ 1 \ 0]^T p_0$ and $\mathbf{P}^2 = [-1 \ 0 \ 0]^T p_0$, respectively. Each needle domain is modelled as an effective edge dislocation, $\mathbf{b} = (3\sqrt{2}\varepsilon_0w/2) [1 \ 1 \ 0 \ 0]$, coupled with generalized line charge $\mathbf{Q} = [0, 0, 0, Q]$. The spacing between the needles is $10w$ along the x_1 axis. Six different positions approaching to an edge are selected for needle N_1 , which are $(0, 0)$, corresponding to the centre of the crystal plate, $(50w, 50w)$, $(100w, 100w)$, $(150w, 150w)$, $(200w, 200w)$, and $(230w, 230w)$. When searching for an equilibrium configuration, the tip of needle domain N_1 was fixed, while needle domain N_2 was moved relative to N_1 along the line $x_2 = x_1 - 10w$ and the position with minimum potential energy was identified. The influence of setting the polarization charge Q in the range of $0 - 0.734q$ is studied, as shown in Fig. 4.

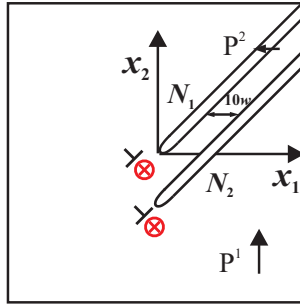


Figure 3: Parallel interacting needle domains in a square crystal plate.

Fig. 4 gives the dimensionless minimum total potential energy of two interacting needle domains with varying effective line charge Q for the different tip positions of needle N_1 . The energy U_E was calculated using Eq. (16), where the corresponding superposition fields of the infinite solution and complementary solution are obtained from Eq. (5). The internal energy U_C due to a single needle domain placed at the centre of the $500w \times 500w$ region is used to nondimensionalize the results. It is found that the minimum potential energy state corresponds to $Q \sim 0.44q - 0.49q$ for the range of positions explored. This result is consistent with the infinite case (no boundaries) studied by Sui and Huber (2020), and justifies adopting the effective line charge $Q = 0.48q$, as in previous work, for subsequent calculations. Note that the potential energy of the pair decreases as they approach the crystal edge at $x_1 = 250w$.

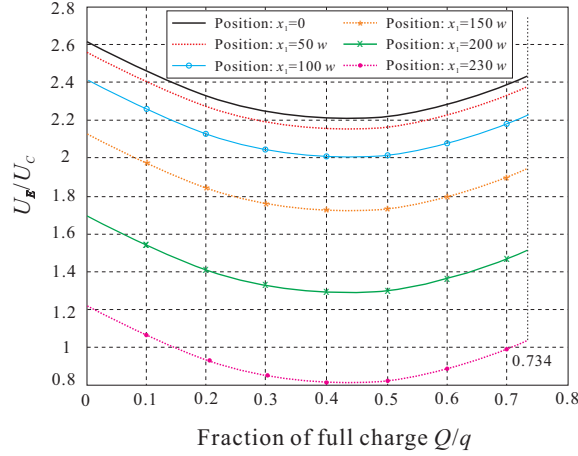


Figure 4: Change of potential energy with respect to the tip position x_1 of needle N_1 and the quantity of effective line charge at the needle tip.

3.3. Fields due to a single needle in a finite crystal

To explore the influence of boundaries on a single needle domain, a 90° a-a needle domain was placed at different positions in the $500w \times 500w$ region. As before, the needle domain has width w and is oriented at 45° to the x_1 positive direction. Its tip position is set in a range from the point $(0, 0)$ to $(240w, 240w)$, on a line along its longitude direction (the line $x_2 = x_1$). The effective charge was set to $Q = 0.48q$ and the effective edge dislocation had Burgers vector $\mathbf{b} = (3\sqrt{2}\varepsilon_0 w/2) [1 \ 1 \ 0 \ 0]$.

To illustrate the effect of the boundary on the needle domain, the change in the contour maps of stress σ_{11} is tracked as the needle tip is placed at the different positions. For comparison, Fig. 5 shows a contour map of stress σ_{11} for the single needle domain in an infinite plate without boundaries. Fig. 6 gives the contour maps of stress σ_{11} for the needle tip located at $(0, 0)$, $(60w, 60w)$, $(160w, 160w)$, and $(220w, 220w)$. The stress fields in both Figs. 5 and 6 are normalized by σ_0 . Note that, in Figs. 6(a)-6(d), the values of stress σ_{11} at the edges $x_1 = -250w$ and $x_1 = 250w$ are always equal to zero, as required by the traction-free boundary condition.

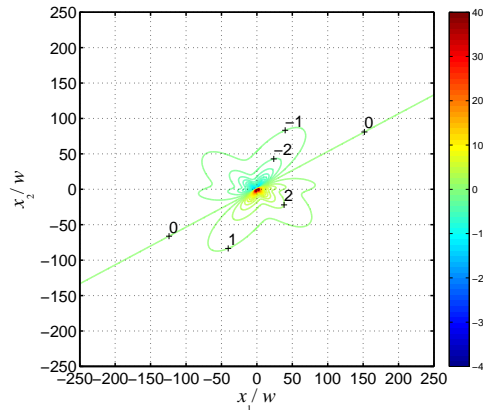


Figure 5: Contour map of stress σ_{11} for a single needle domain in an infinite plate.

Comparing Figs. 6(a) and (b) with the reference case given in Fig. 5, it can be seen that the σ_{11} field close to the needle tip is almost unaffected by the boundary when the needle is near the centre of the plate. As the needle tip approaches the boundary, the influence of the boundary becomes strong, see Figs. 6(c) and 6(d). When the needle tip is well within $100w$ of the boundary, as in Fig. 6(d), the stress gradient

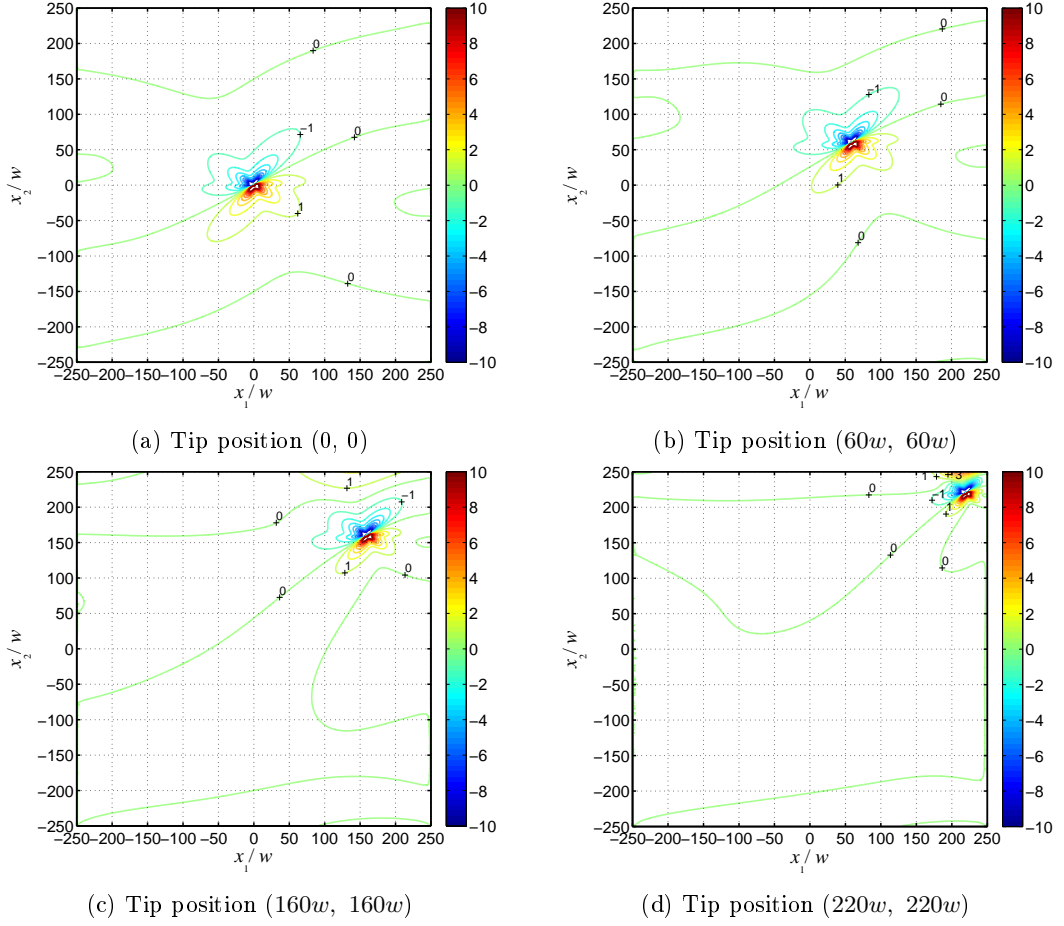


Figure 6: Stress σ_{11} fields produced by a single needle domain located at various positions in a finite plate.

around the tip is greatly increased, compressing the needle-tip fields. Here, there is significant tensile stress ($\sim 3\sigma_0$) on the upper boundary ($x_2 = 250w$) and the pattern of stress field is altered by comparison with the infinite plate. This indicates the significance of accounting for free surfaces when the tip of a needle domain is within about 100 needle widths of a free surface.

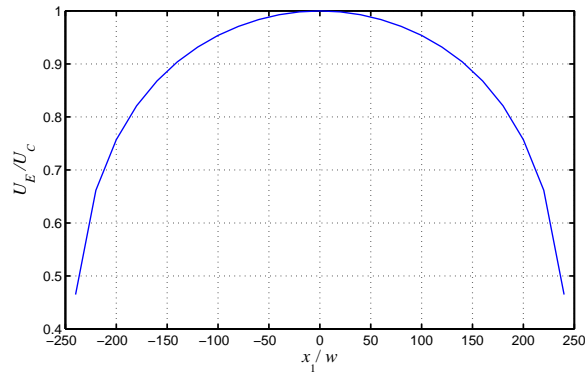


Figure 7: Change in potential energy as the needle domain approaches to an edge.

Fig. 7 shows the change of non-dimensional potential energy (U_E/U_C), as the needle tip varies in distance

from the boundary, calculated using Eq. (16). Evidently the internal energy is maximised when the needle tip is at the plate centre, indicating that there is a force of attraction towards the boundaries, as found for dislocations in uncoupled isotropic media. This leads to the formation of domain stripe patterns, where the eventual equilibrium state consists of multiple layers of domains with no (or few) needle-tips present. However, if there is lattice resistance or any form of domain wall pinning, then needles may terminate within a crystal in equilibrium. If the lattice resistance is uniform, there will be a corresponding size of region adjacent to the free boundaries in which needle tips are not found. This is consistent with the experimental observations of Potnis and Huber (2013) and an example of such a band free of needle-tips appears later in this paper at Fig. 13.

3.4. A pair of needle domains in a finite crystal

Next, return to the case of a pair of parallel needle domains (N_1 & N_2) oriented at 45° to the x_1 positive direction, and separated by $10w$ along the x_1 direction, see Fig. 3. Each needle domain is modelled as an effective edge dislocation and line charge, using $Q = 0.48q$. The needle N_1 is placed at each of three different initial positions: at the centre $(0, 0)$, a near-center position $(50w, 50w)$ and a near-boundary position $(200w, 200w)$, respectively. The needle N_2 is moved relative to N_1 along the line $x_2 = x_1 - 10w$. Fig. 8 shows the resulting normalized extension force acting on each needle and the normalized total energy due to the two interactive needle domains.

Fig. 8(a) shows the variation in extension forces on the two needle domains as the needle N_2 moves, with N_1 fixed at the origin. Note that, in this case, the extension forces acting on the two needles have equal magnitude but opposite sign. The same result appears in the case of two needle domains in an infinite crystal plate. This can be explained by considering Eq. (17), where the (\wedge) terms come from the contribution of the image field which depends on the boundaries, while the other terms give the force that would be experienced in the infinite plate. If the needles are sufficiently far from the boundaries, the (\wedge) terms become negligible and the interaction matches that in an infinite plate. In addition, Fig. 8(a) shows three equilibrium positions, labelled a1, a2, and a3. However, only position a2 is stable for both needle domains, corresponding to a minimum energy. This stable configuration implies that needles far from the boundary can form a comb structure with the tips aligning on the line $x_2 = -x_1$, at 45° to the x_1 -axis, as in the case of the infinite crystal studied by Sui and Huber (2020).

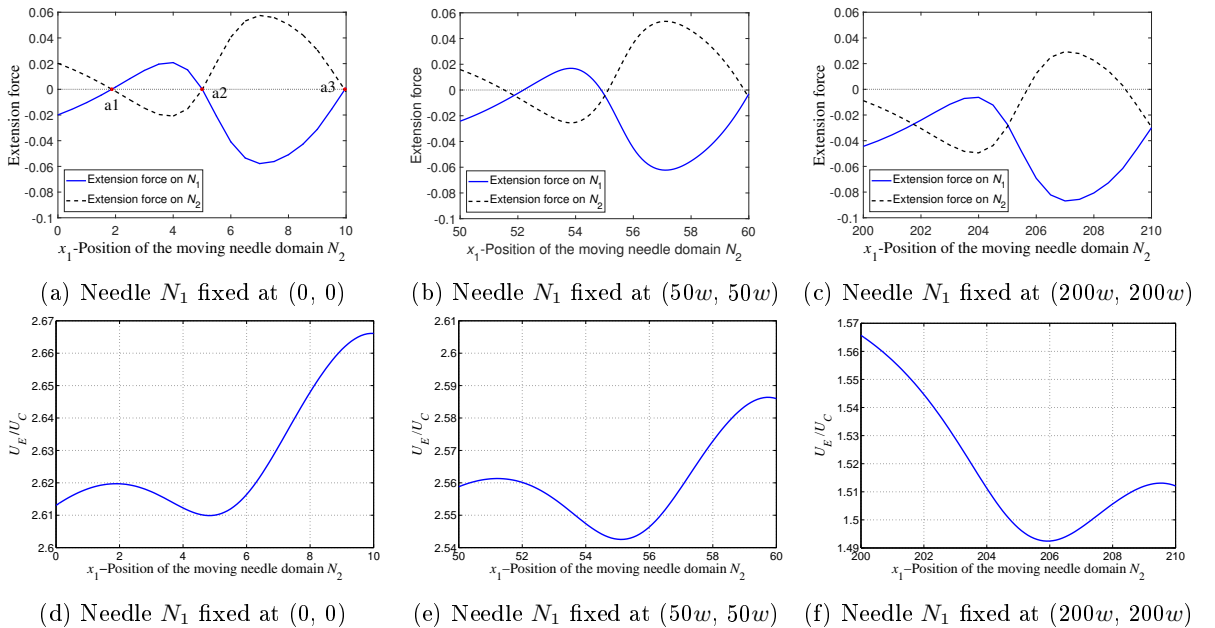


Figure 8: Extension forces and the potential energy for two interactive needle domains with spacing $10w$ when needle N_1 is fixed at $(0, 0)$ $(50w, 50w)$ and $(200w, 200w)$, respectively.

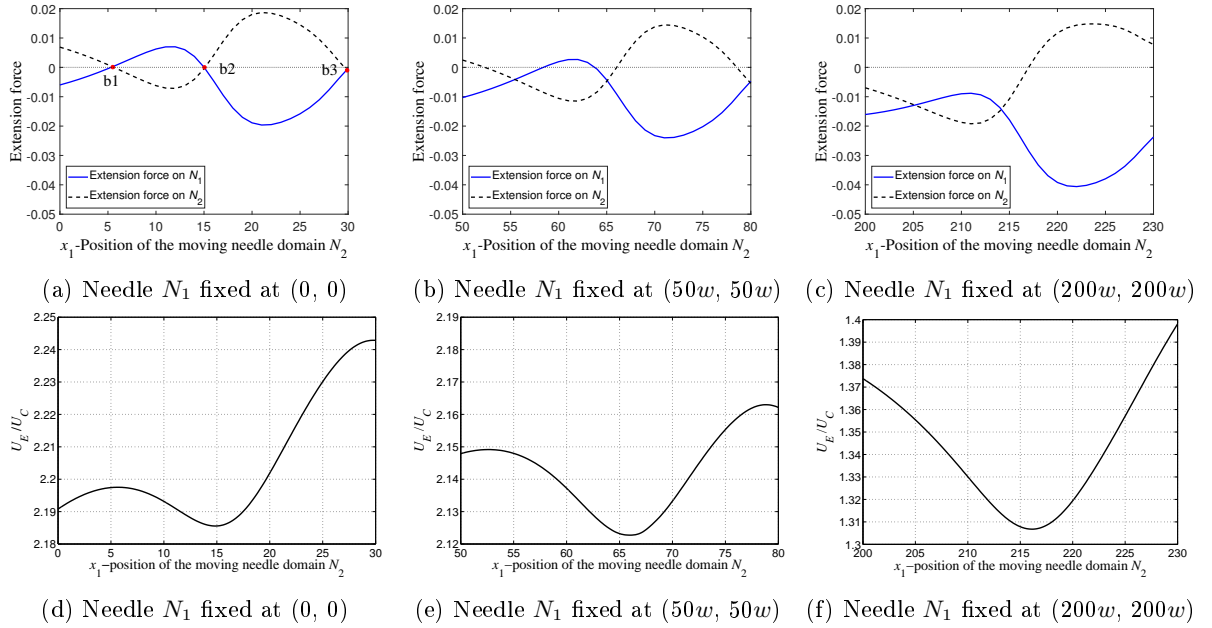


Figure 9: Extension forces acting on two needle domains with spacing $30w$ when needle N_1 is fixed at $(0, 0)$ $(50w, 50w)$ and $(200w, 200w)$.

With needle N_1 displaced away from the centre, at $(50w, 50w)$ or $(200w, 200w)$, the corresponding extension force and the potential energy are shown in Figs. 8(b), 8(e) and 8(c), 8(f). Shortening the needle domains by moving their tips towards the boundary shifts the extension forces towards negative values, driving the needle-tips towards the nearest edge. There is now no equilibrium position for both the needle domains, unless lattice friction or some other resistance is present to hold them in place. If one needle is pinned, it can hold the other in place. Comparing the potential energy of the pair of needles in various positions, it can be seen that the potential energy well of Fig. 8(f) is deeper than the other two cases, suggesting that proximity to the boundary stabilizes the needle pattern, whilst imposing a net attraction on the pair towards the boundary.

Based on the wedge-shaped tip configuration of experimentally observed needle domains, Sui (2015) argued that the lattice friction corresponds to a maximum resistance force F_{cr} of about 0.05 in normalized units. With this lattice resistance, the pair of needle domains can reach equilibrium in any configuration where the extension force on both needle domains has magnitude less than F_{cr} . Referring to Figs. 8(b) and 8(c), this gives a range of stable positions. Now, assuming needle N_1 to be fixed by lattice friction enables a minimum energy position for N_2 to be found, indicating a line along which a set of several needle tips could lie in equilibrium provided the first in the line is held by lattice friction. Far from the boundary, the orientation of this line is at 45° to the x_1 axis, but, as the group approaches an edge, this angle reduces to less than 30° .

Additionally, we select a pair of needle domains with wider spacing, $30w$, to compare with the needle domains spaced at $10w$. As before, the tip of needle N_1 is fixed at $(0, 0)$, $(50w, 50w)$ or $(200w, 200w)$ and the tip of needle N_2 is moved, now on the line $x_2 = x_1 - 30w$. Figs. 9(a)-9(f) present the resulting variation of extension force and potential energy for both needle domains in this case. The results are similar in character to the case with spacing of $10w$ but note that there are significant differences. The interaction forces are now smaller, and remain less than F_{cr} over a wide range of positions. Meanwhile the size of the perturbation needed to escape the energy well in which N_2 is found, as indicated by the distance between minimum and maximum energy positions for N_2 , has increased. Consequently, lattice friction will hold a widely spaced comb of needles in place more easily than it will narrowly spaced combs of needles. Fig. 9(c) also illustrates the change in shape of the interaction force curve as one of the needle tips becomes close to the edge of the crystal plate.

4. Evolution of combs of needles under mechanical loads

In this section, the evolution of a comb-like array of needles in a thin crystal plate under compressive loading is discussed. Such combs of needles are commonly found in ferroelectrics and their propagation is a mechanism for ferroelectric or ferroelastic switching. An array of comb-like needle domains comprising 11 needles, as shown in Fig. 10, is modelled. Their tips are initially located on the line $x_2 = -x_1$ oriented at $\theta = 45^\circ$ to the negative x_1 axis. The spacing of the needle domains is $10w$ along the x_1 direction. Compression is applied parallel to the x_1 axis in increments. At each loading step, needle domains are allowed to extend (or retract) at a rate proportional to the total driving force for extension. Equilibrium is reached when the driving force on all needles is less than $F_{cr} = 0.05$ in normalized units, and no needle moves unless its driving force exceeds F_{cr} in magnitude. Once equilibrium is reached, the load is incremented to the next step and the process is repeated. Nucleation of new needle domains is not included in the current model. The boundary conditions are given as follows: At $x_1 = \pm 250w$, T_0 is a compressive stress increasing from 0 to 2.6 MPa in steps of 0.02 MPa, and $\phi_0 = 0$ corresponding to electroded surfaces in short-circuit condition. At $x_2 = \pm 250w$, the edges are traction free and charge free, corresponding to free surfaces in an insulating medium.

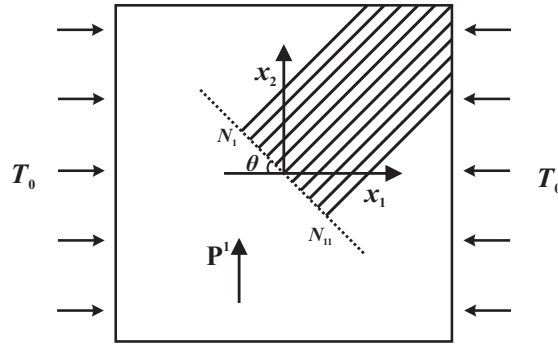


Figure 10: A comb-like array of needle domains under compressive loading.

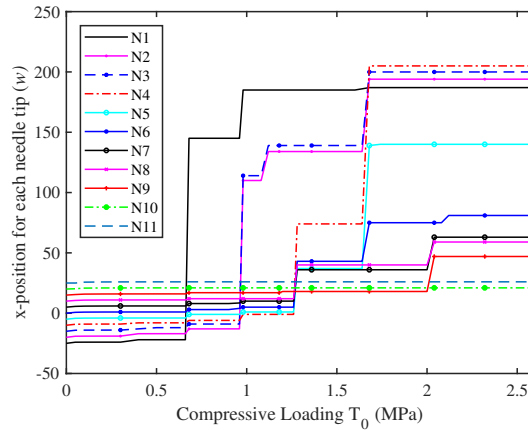


Figure 11: Evolution of comb-like needle domains under the compressive loading.

The evolution of needle domains results from polarization switching due to the external loading; in this loading case, the compressive loading generally causes the needles to retract. Fig. 11 shows the changes of tip position of each needle in the comb-like pattern as loading proceeds. The corresponding patterns of needle domains at various load levels are shown in Fig. 12, where a dotted line at $x_2 = -x_1$ indicates the initial location of the needle-tips. Each pattern in Fig. 12 is in equilibrium. Fig. 12(a) shows that when

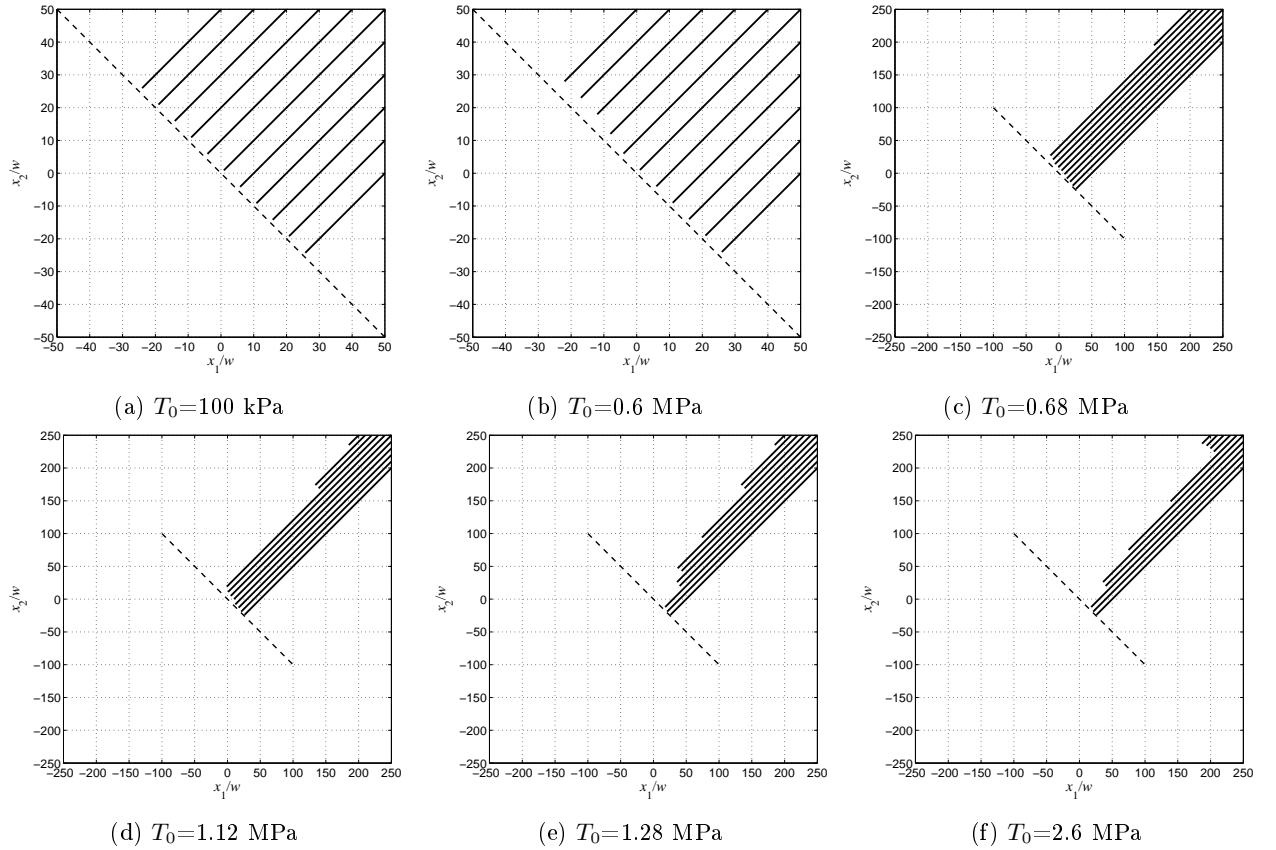


Figure 12: Evolution of comb-like needle domains under compressive loading.

the external load reaches 100 kPa, only a slight reduction in length ($< 1w$) is seen in each of the needle domains. A similar small change in needle tip positions was observed in experiments by Potnis and Huber (2013) using compressive loading. As the load increases to 0.6 MPa, the needle-tip displacements remain small ($< 4w$). However, at 0.68 MPa, the needle N_1 at the upper edge of the comb suddenly retracts by more than $100w$ towards the boundary. The rest of the comb remains largely unchanged until the compressive load increases to about 1 MPa, when the needles N_2 and N_3 escape from the tip front line and retract toward the boundary in large jumps, see Fig. 12(d). The needle domains successively break free from the comb as the external load is increased. Finally, a stepped pattern forms, composed of needle domains in groups of different lengths, as seen in Fig. 12(e) and 12(f). Similar stepped structures can be observed in real crystals as shown in Fig. 13, though in this case the pattern developed during thermal processing and the mechanical conditions are not known. In particular, groups of aligned needle tips are seen and these groups show different lengths of needle. It is also found in experiments that individual needle domains can suddenly retract or disappear under mechanical loading when a critical load level is reached, while others are not affected or move only slightly at the same load level.

As a final illustration of the model, consider whether pinning a small number of domain needles in a fixed position can prevent the comb structure from breaking up under load. When the simulation was repeated with needle N_1 fixed, the pattern remained stable until T_0 reached 0.76 MPa, at which point needle N_2 retracted, see Fig. 14(a). If both N_1 and N_2 are fixed, the comb remains stable up to $T_0 = 1.06$ MPa, when needles N_3 and N_4 break away simultaneously. Comparing to the unpinned comb of needle domains, the pinned comb is more stable to loading, but fixing a few needles does not prevent break up. A stepped structure still develops.

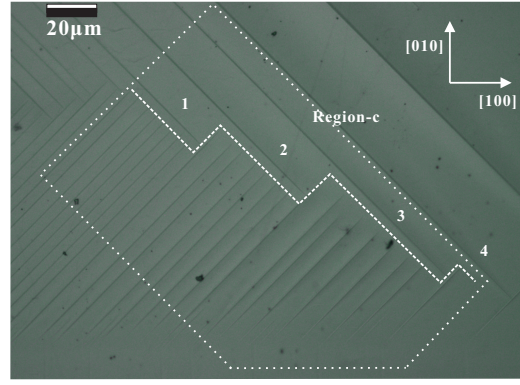


Figure 13: A stepped pattern of needle domains in a BaTiO₃ crystal plate.

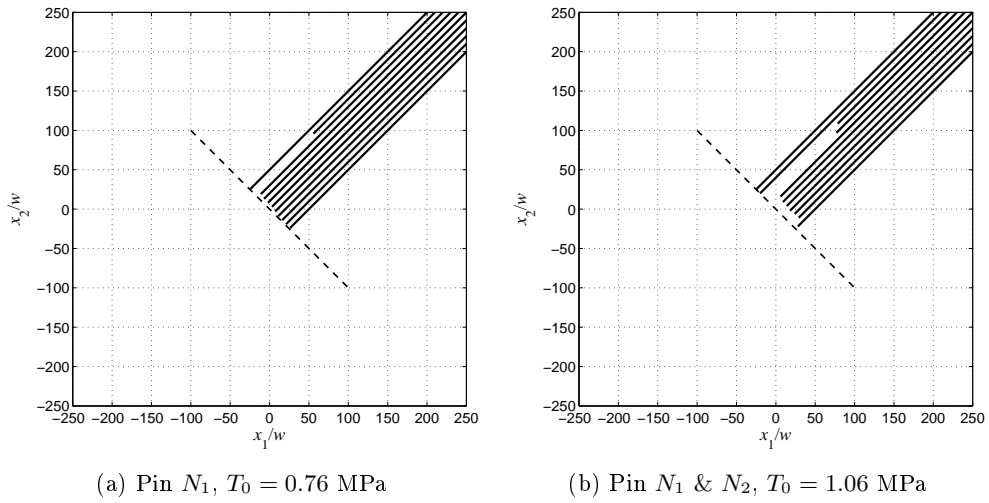


Figure 14: Evolution of comb-like needle domains with one or more needle-tips fixed in place. (a) The needle N_1 is pinned, (b) the needles N_1 and N_2 are pinned.

5. Conclusions

A model of needle domains in ferroelectrics was developed in which the fields due to the needle domains are represented by the coupled fields of an effective dislocation and line charge. Superposition theory was then adopted to analyse the effect of boundary conditions on a finite material region containing needle domains. This showed that needle domains experience a driving force attracting their tips to nearby free boundaries, which is consistent with the observation that domains are often found in the form of complete laminations, rather than as needles. For a needle to terminate within a crystal in stable equilibrium, it must be constrained in some way: either by external loading, residual stress, lattice friction or some other form of pinning. In practice, a modest degree of lattice friction is sufficient to stabilise many patterns of needle domains provided the tips are not too close to a free boundary. The model enables the interaction of groups of needle domains in a finite crystal to be simulated. This was illustrated using the example of a pair of parallel needle domains, where it is found that interaction with free boundaries changes the stable equilibrium positions, but if the needle tips are far from boundaries a simple model of an infinite crystal retains good accuracy. The evolution of comb-like patterns of needle domains was simulated under the action of compressive loads. Here, at low levels of loading, a slight motion of the needle tips was found, while greater loads generated bursts of activity in which the comb rearranged into a stepped pattern.

It should be noted that the model neglects a number of significant effects. The material inhomogeneity

introduced by the presence of multiple domains was neglected, and screening of charge was assumed to occur in a simplified way that reduces the effective line charge at each needle domain. Nucleation of new domains was neglected, as was the intersection of needle domains growing in different directions (all the examples given have only parallel needles). Extending the model to these situations would require the development of suitable rules that capture the physics of the interactions. Despite several simplifications, the results show some subtle features of the evolution of needle domain patterns that are qualitatively consistent with observed features of the real materials. The superposition model thus provides a promising route for the investigation of macroscopic needle domains and their evolution under external loads.

6. Acknowledgements

The authors are grateful for the financial support from the EPSRC of UK under Grant No. EP/G065233/1 and the Fundamental Research Funds for the Central Universities of China under Grant No. G2019KY05207.

7. Appendix

The material matrices Q_{KS} , S_{KS} , and B_{KS} in the Barnett and Lothe integral formalism Barnett and Lothe (1975) are:

$$Q_{KS} = -\frac{1}{2\pi} \int_0^{2\pi} (nn)_{SK}^{-1} d\theta \quad (24)$$

$$S_{KS} = -\frac{1}{2\pi} \int_0^{2\pi} (nn)_{KJ}^{-1} (nm)_{JS} d\theta \quad (25)$$

$$B_{KS} = \frac{1}{8\pi^2} \int_0^{2\pi} \{ (mm)_{KS} - (mn)_{KJ} (nn)_{JR}^{-1} (nm)_{RS} \} d\theta \quad (26)$$

Vectors \mathbf{m} and \mathbf{n} are defined in terms of a plane orthogonal basis (\mathbf{i}, \mathbf{j}) by

$$\mathbf{m}(\theta) = \mathbf{i} \cos \theta + \mathbf{j} \sin \theta \quad (27)$$

$$\mathbf{n}(\theta) = -\mathbf{i} \sin \theta + \mathbf{j} \cos \theta \quad (28)$$

The components of the 4×4 matrices (\mathbf{nn}) and (\mathbf{nm}) are defined by

$$(ab)_{JK} = a_i E_{iJKm} b_m \quad (29)$$

where, a and b any are real three-dimensional vectors. Here lower-case indices run from 1 to 3 while upper-case indices run from 1 to 4. The group of tensors represented by E_{iJKm} is:

$$\begin{aligned} E_{iJKm} &= C_{ijk m} \quad (J, K = 1, 2, 3) \\ &= e_{mij} \quad (J = 1, 2, 3; K = 4) \\ &= e_{ikm} \quad (J = 4; K = 1, 2, 3) \\ &= -\kappa_{im} \quad (J = K = 4) \end{aligned} \quad (30)$$

8. Bibliography

References

- Barnett, D.M., Lothe, J., 1975. Dislocations and line charges in anisotropic piezoelectric insulators. *Physica Status Solidi (b)* 67, 105–111.
- Bhattacharya, K., Ravichandran, G., 2003. Ferroelectric perovskites for electromechanical actuation. *Acta Materialia* 51, 5941–5960.
- Blackburn, J.F., Salje, E.K.H., 1999. Formation of needle shaped twin domains in cordierite: a computer simulation study. *Journal of Applied Physics* 85, 2414–2422.
- Bornarel, J., 1972. Existence of dislocations at domain tips in ferroelectric crystal KH_2PO_4 . *Journal of Applied Physics* 43, 845–852.

- Bornarel, J., Lajzerowicz, J., 1968. Experimental evidence for the long-range interaction of domains in ferroelectric KH_2PO_4 . *Journal of Applied Physics* 39, 4339–4341.
- Burcu, E., Ravichandran, G., Bhattacharya, K., 2004. Large electrostrictive actuation of barium titanate single crystals. *Journal of the Mechanics and Physics of Solids* 52, 823–846.
- Carka, D., Landis, C.M., 2012. Equilibrium conditions and evolution of needle domain arrays in ferroelectric single crystals. *ASME 2012 Conference on Smart Materials, Adaptive Structures and Intelligent Systems* 2, 255–257.
- Fang, D.N., Jiang, Y.J., Sun, C.T., 2007. Interactions between domain switching and crack propagation in poled BaTiO_3 single crystal under mechanical loading. *Acta Materialia* 55, 5758–5767.
- Harrison, R.J., Redfern, S.A.T., Salje, E.K.H., 2004. Dynamical excitation and anelastic relaxation of ferroelastic domain walls in LaAlO_3 . *Physical Review B* 69, 144101.
- Harrison, R.J., Salje, E.K.H., 2010. The noise of the needle: avalanches of a single progressing needle domain in LaAlO_3 . *Applied Physics Letters* 97, 021907.
- Li, W.Y., Landis, C.M., 2010. Modeling of the nucleation and growth of domain needles. *ASME 2010 Conference on Smart Materials, Adaptive Structures and Intelligent Systems* 1, 373–374.
- Li, W.Y., Landis, C.M., 2011. Nucleation and growth of domains near crack tips in single crystal ferroelectrics. *Engineering Fracture Mechanics* 78, 1505–1513.
- Li, Z., Chan, S.K., Grimsditch, M.H., Zouboulis, E.S., 1991. The elastic and electromechanical properties of tetragonal BaTiO_3 single crystals. *Journal of Applied Physics* 70, 7327–7332.
- Lich, L., Dinh, V., 2019. Formation of polarization needle-like domain and its unusual switching in compositionally graded ferroelectric thin films: an improved phase field model. *RSC Advances* 9, 7575.
- Liu, Z., Schold, E., Karpov, D., Harder, R., Lookman, T., Fohntung, E., 2020. Needle-like ferroelastic domains in individual ferroelectric nanoparticles. *Advanced Electronic Materials* 6, 1901300.
- Matsumoto, T., Okamoto, M., 2010. Ferroelectric 180° a-a nanostripe and nanoneedle domains in thin BaTiO_3 films prepared with focused-ion beam. *IEEE Transactions on Ultrasonics, Ferroelectrics, and Frequency Control* 57, 2127–2133.
- Moore, K., Conroy, M., O'Connell, E., Cochard, C., Mackel, J., Harvey, A., Hooper, T., Bell, A., Marty Gregg, J., Bangert, U., 2020. Highly charged 180° head-to-head domain walls in lead titanate. *Communications Physics* 3, 231.
- Nataf, G., Salje, E., 2020. Avalanches in ferroelectric, ferroelastic and coelastic materials: phase transition, domain switching and propagation. *Ferroelectrics* 569, 82–107.
- Neumeister, P., Kessler, H., Balke, H., 2010. Effect of switching stresses on domain evolution during quasi-static crack growth in a ferroelastic single crystal. *Acta Materialia* 58, 2577–2584.
- Potnis, P., Huber, J., 2013. In-situ observation of needle domain evolution in barium titanate single crystals. *Journal of the European Ceramic Society* 33, 327–333.
- Qi, X.Y., Liu, H.H., Duan, X.F., 2006. In situ transmission electron microscopy study of electric-field-induced 90° domain switching in BaTiO_3 single crystals. *Applied Physics Letters* 89, 092908.
- Salje, E.K.H., 2021. Mild and wild ferroelectrics and their potential role in neuromorphic computation. *APL Materials* 9, 010903.
- Salje, E.K.H., Ishibashi, Y., 1996. Mesoscopic structures in ferroelectric crystals: needle twins and right-angle domains. *Journal of Physics: Condensed Matter* 8, 8477–8495.
- Sui, D., 2015. Modelling and experimental observation of ferroelectric domains. DPhil thesis, University of Oxford.
- Sui, D., Huber, J.E., 2020. Modelling and interaction of needle domains in barium titanate single crystals. *European Journal of Mechanics/ A Solids* 80, 103919.
- Tagantsev, A.K., Cross, L.E., Fousek, J., 2010. Domains in ferroic crystals and thin films. Springer-Verlag New York, Inc.
- Zhang, Z.H., Qi, X.Y., Duan, X.F., 2006. Direct determination of the polarization direction of domains in BaTiO_3 single crystal. *Applied Physics Letters* 89, 242905.
- Zhang, Z.H., Qi, X.Y., Duan, X.F., 2008. Two-step evolution mechanism of multi-domains in BaTiO_3 single crystal investigated by in situ transmission electron microscopy. *Scripta Materialia* 58, 441–444.